Solid State Ionics 353 (2020) 115377

Contents lists available at ScienceDirect

Solid State Ionics

journal homepage: www.elsevier.com/locate/ssi

High power iron phosphate cathodes by atomic layer deposition

Anders Brennhagen*, Kristian B. Kvamme, Katja S.S. Sverdlilje, Ola Nilsen*

Centre for Materials Science and Nanotechnology (SMN), Department of Chemistry, University of Oslo, P.O. Box 1033, Blindern, N-0315 Oslo, Norway

ARTICLE INFO

Keywords:
Atomic layer deposition
Thin films
Iron phosphate
Li-ion batteries
Cathode material
High power

ABSTRACT

Amorphous thin films of $FePO_4$ and $Fe_4(P_2O_7)_3$ show excellent power capabilities and good stability as cathode materials in Li-ion batteries. Within our tested range of materials, 10 nm $FePO_4$ shows the best results and can handle specific powers above 1 MW/kg. The thin films are deposited using atomic layer deposition (ALD) and we studied the growth using in situ quartz crystal microbalance (QCM) showing self-limiting growth. Their electrochemical properties were characterized as cathode materials in coin cell batteries using cyclic voltammetry (CV) and galvanostatic cycling (GC), correcting for the roughness of the substrates and addressing contributions from non-Faradaic processes.

1. Introduction

As the degree of electrification continuously increases, the need for better and more specialized batteries follows. Li-ion battery technology is leading for energy storage today because of the high energy density and relatively high power capabilities, but there is still plenty of room for improvements, particularly with respect to high power and safety aspects. These are aspects where thin film technology can be applicable, both for controlled design of interfaces, avoiding extra additives and for realization of all-solid-state batteries.

$LiFePO_4$ (LFP) is a cheap and environment friendly battery material with minimal volumetric variation during cycling, providing long life time and opens up for high-power applications [1]. It is currently the most used cathode material worldwide [2]. Commercial LFP batteries use nanoparticles of $LiFePO_4$, but other methods for nanostructuring have also been tested [3–5]. The majority of LFP materials used are of the Pnmb orthorhombic structure, whereas its amorphous version has been much less studied. Gandrud et al. have synthesized and investigated amorphous thin films of $FePO_4$, which showed very high power capabilities, above 1 MW/kg, and had good cycling stability [6,7].

While the LFP material has been widely studied, the other phases present in the Fe-P-O system has received limited attention. The phase diagram of the Fe-P-O system includes the phases $FePO_3$, Fe_3PO_7, Fe_2O_3, $Fe_4(P_2O_7)_3$ and $FePO_4$ [8], where a few reports exist on the first three, evidencing interesting properties as anode materials, although with various shortcomings in cycling stability [9–11]. To our best knowledge, there are no reports on the electrochemical properties of the $Fe_4(P_2O_7)_3$ phase, but Nishimura et al. have investigated $Li_2FeP_2O_7$ as a cathode material where they managed to obtain the full theoretical capacity of 110 mAh/g [12]. The material has a potential of 3.5 V vs Li, which is the highest known potential for an iron based phosphate cathode, and it showed good stability.

In this study, we have revisited the work of Gandrud et al. [6,7] with deposition of thin films of amorphous $FePO_4$ and performed more accurate electrochemical characterizations. It became clear through the study that the observed capacity comes from a combination of redox reactions and electrostatic charge accumulation. We here term these two different contributions Faradaic capacity (redox reactions) and non-Faradaic capacity (electrostatic charge accumulation). We have also investigated thin films of amorphous $Fe_4(P_2O_7)_3$ and compared the electrochemical properties of these two materials. We produced the films by atomic layer deposition (ALD) and studied the deposition process by in situ quartz crystal microbalance (QCM).

2. Experimental

We grew the thin films in an F-120 Sat reactor (ASM Microchemistry Ltd) using $Fe(thd)_3$ (sublimed grade, Volatec), $MePO_4$ (98%, Merck), H_2O (> 1 MΩ·cm) and O_3 as precursors. The ozone was produced with an AC-2025 ozone generator from In USA from O_2 gas (99.5%, Praxair). The product was a mixture of O_3 and O_2 with a concentration of ca. 12 wt% O_3. We kept the sublimation temperature for $Fe(thd)_3$ at 100 °C while the other precursors were introduced to the reaction chamber from room temperature using external bubblers. For material characterization, we used Si substrates (UniversityWafer) while we used steel substrates (CR20, 316, Pi-Kem) for electrochemical characterization. The steel substrates were polished with P2400 grit SiC abrasive

* Corresponding authors.
E-mail addresses: anders.brennhagen@smn.uio.no (A. Brennhagen), ola.nilsen@kjemi.uio.no (O. Nilsen).

https://doi.org/10.1016/j.ssi.2020.115377
Received 13 November 2019; Received in revised form 28 May 2020; Accepted 2 June 2020

Table 1
Pulse and purge times used in depositions of iron phosphate thin films.

Precursor	Pulse time (s)	Purge time (s)
$Fe(thd)_3$	1.5	1.5
O_3	4.0	5.0
Me_3PO_4	4.0	3.0
$O_3 + H_2O$	6.0	8.0

paper to reduce surface roughness before deposition. The pressure inside the reactor was kept between 3.0 and 3.5 mBar during the depositions, using a N_2 gas flow of 200 cm^3/min in the external chamber and 300 cm^3/min over the substrates. All films were deposited at 250 °C using the pulsing parameters listed in Table 1, apart from the QCM investigation using excessive pulsing and purging, Fig. 2.

2.1. Materials characterization

The QCM setup was based on home built holders for gold coated 6 Mhz α-quartz crystals (AT-cut, INFICON) and logged using a Colnatec EON-LT. The signal was converted to ng/cm^2 through use of internal standards of deposition of Al_2O_3 throughout the deposition campaign. We used a Woollam alpha-SE ellipsometer to measure the thickness of the films by fitting the data to a Cauchy function, and a D8 Discover X-ray diffractometer with a Cu Kα1 source and Bragg-Brentano geometry from Bruker to characterize for crystallinity. The composition of iron and phosphorus in the films was determined by X-ray fluorescence (Axios Minerals, Panalytical) using a standardless method. We used an S Neox non-contact optical profiler from Sensofar to measure the roughness of the steel substrates.

2.2. Electrochemical characterization

The mass of the deposited cathode thin films was determined using the thickness obtained from spectroscopic ellipsometry and the density obtained from XRF, with corrections using the area factor (surface area divided by projected area) obtained from optical profilometry. To perform electrochemical characterization of the thin films we built CR2032 coin cell batteries with stainless steel parts (304, Pi-Kem), in a LABmaster SP glovebox from MBRAUN with Argon atmosphere (99.999%, Praxair). We used 1 M $LiClO_4$ (99.99%, Sigma-Aldrich) in a 1:1 mixture of ethylene carbonate (EC) (99%, Sigma-Aldrich) and dimethyl carbonate (DMC) (≥99%, Sigma-Aldrich) as electrolyte and Li-metal (≥99.9%, China Energy Li CO) as reference anode. We performed galvanostatic cycling (GC) and cyclic voltammetry (CV) with an MPG2 research grade battery tester from Bio-Logic. For both techniques we used a voltage range of 2.00–4.00 V for testing of $FePO_4$ and 2.50–4.25 V for $Fe_4(P_2O_7)_3$. In CV measurements, we used a sweep rate of 0.1 mV/s and in GC measurements we applied currents in the range of 20–5120 μA.

3. Results and discussion

3.1. Materials characterization

Suitable pulsing and purging parameters for deposition of $FePO_4$ were determined using QCM analysis based on the growth rate of 20 cycles of each configuration. While testing one parameter the others were kept constant. The pulsing parameters should be as short as possible while still providing saturated growth. Fig. 1 shows the growth rate as a function of pulse/purge times for each of the precursors. All precursors show saturation within the ranges tested and led to the parameters listed in Table 1 in the Experimental section.

To study the growth in more detail we extended the parameters and focused on the average response from 20 cycles, Fig. 2. During the Fe $(thd)_3$ pulse (1), we obtained a large mass increase as expected due to the high mass of the molecule. We assume that it released one or two of the thd ligands when it reacted with the surface. The curves do not show as clear a saturation as given in Fig. 1, however, it should be kept in mind that excess pulsing may affect the other parameters used. During the $Fe(thd)_3$ purge (2), we observed a small decrease in mass, which probably represents the removal of physisorbed $Fe(thd)_3$. The mass reduction observed during the O_3 pulse is significantly larger than what is expected for oxygen replacing thd groups, as the graph drops below zero (3). This is most probably an artefact from the exothermal decomposition reaction of ozone, which may be interpreted as a reduction in mass. This is corroborated by the apparent increase in mass during the following purge (4). During the Me_3PO_4 pulse, the precursor attached to the surface while releasing one or two methyl groups, leading to a mass increase (5). When pulsing $H_2O + O_3$, we would expect that oxygen replaced the remaining methyl groups with the result of a small mass reduction. However, we obtained a signal indicating a large mass increase (7). As Diskus et al. has shown, the growth rate may be different when pulsing H_2O together with O_3, compared to a pure O_3 pulse [13]. This effect does, however, not explain the apparent mass increase. We therefore assume that the observed mass increase is due to absorption of H_2O into the film, which is also released during the following purge (8). At the end of the cycle (9), we obtained a growth of 57 ng/cm^2, which is slightly above the average of 44 ng/cm^2/cycle observed for the optimized pulsing times, Fig. 1.

For deposition of the iron phosphate thin films, we used a combination of the binary processes: $[Fe(thd)_3 + O_3]$ and $[Me_3PO_4 + (H_2O + O_3)]$. By varying the ratio between these two combinations, we obtained the film compositions and growth rates shown in Fig. 3. A 1:1 composition, corresponding to $FePO_4$, was obtained with a pulsing ratio of 3:1 and we used a 3:2 pulsing ratio to obtain the composition corresponding to $Fe_4(P_2O_7)_3$. The growth rate of the films was sensitive to the pulsing ratio used. This is probably related to the density of the deposited films, where we obtained 3.2 g/cm^3 for $FePO_4$ and 2.8 g/cm^3 for $Fe_4(P_2O_7)_3$ from XRF measurements.

Both systems show a linear dependence between thickness and the number of subcycles used, Fig. 4, indicating a stable ALD growth without significant development of texture.

X-ray diffraction (XRD) analysis of the films proved no visible peaks, even on a logarithmic scale, apart from the peaks induced by the silicon substrate (marked *), Fig. 5. This indicates that the thin films are amorphous as deposited.

Prior to deposition, we used an optical profiler to investigate the surface of our polished and unpolished steel substrates used for electrochemical characterization. The unpolished steel spacer showed a notably larger roughness than the polished steel spacer, Fig. 6. The unpolished steel spacer gave an RMS roughness of 0.27 ± 0.03 μm and an area factor of 2.1 ± 0.2, while the polished steel spacer gave an RMS roughness of 0.20 ± 0.03 μm and an area factor of 1.8 ± 0.1. This factor must be taken into account when calculating the total mass of the thin films for determination of specific capacity.

3.2. Electrochemical characterization

Cyclic voltammograms of 40 nm $Fe_4(P_2O_7)_3$ and 30 and 1 nm $FePO_4$, show very broad redox peaks, Fig. 7, in line with the amorphous structure of the film (as shown by XRD analysis). The peaks remain broad throughout the cycling, indicating that the amorphous structure is conserved. This is also supported by earlier studies [6,7]. One notable difference between the two materials is that the redox peaks for $Fe_4(P_2O_7)_3$ is occurring at slightly higher voltages. This is also the reason why we used a slightly higher voltage range during CV analysis for this material. Still, both materials show electrochemical potentials roughly between 3.00 and 3.25 V, which is lower than the literature values for $Li_2FeP_2O_7$ of 3.50 V and $FePO_4$ of 3.45 V [1]. Application of the 1 nm $FePO_4$ is meant to correspond to the effects from the surface of

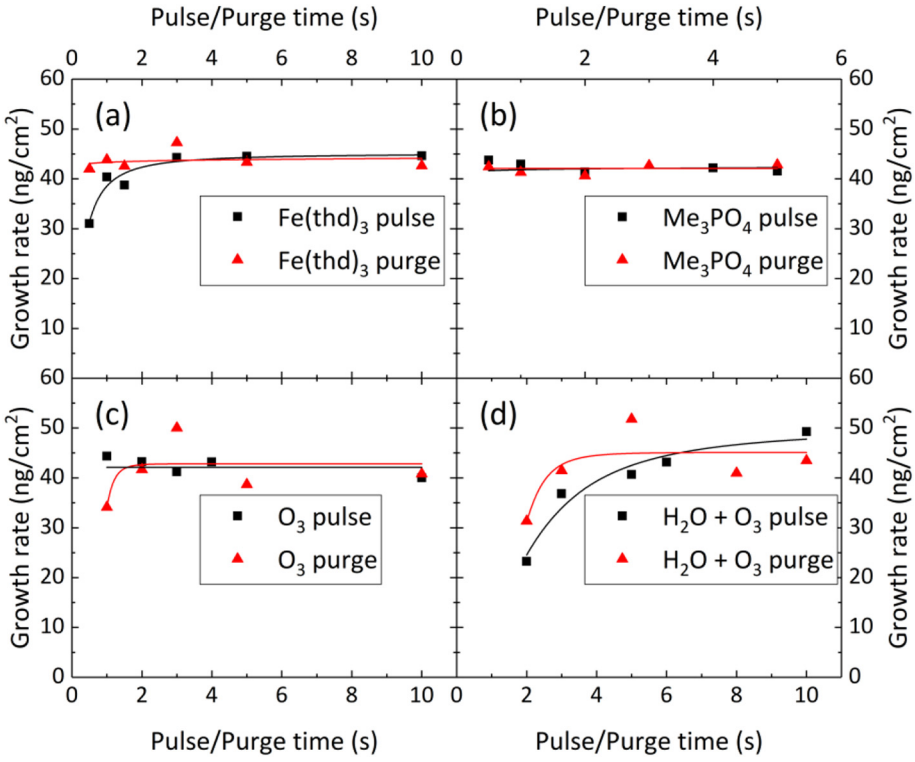

Fig. 1. Growth rate vs pulse/purge times for (a) $Fe(thd)_3$, (b) Me_3PO_4, (c) O_3 and (d) $H_2O + O_3$ with added trend lines. One specific parameter was changed at a time, while all other parameters where kept constant and equal to the parameters listed in Table 1 in the Experimental section.

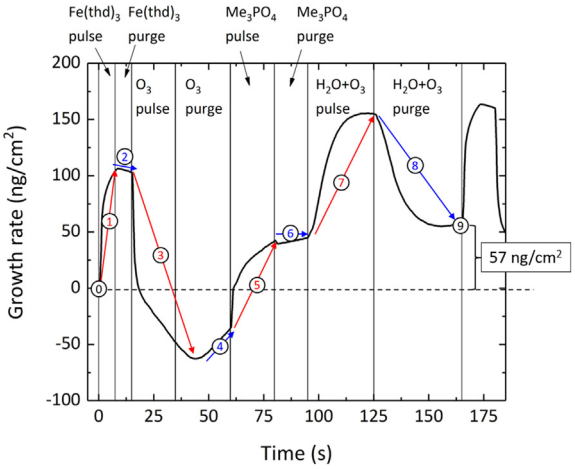

Fig. 2. Detailed analysis of the average QCM signal from 20 cycles of deposition of iron phosphate with extended pulsing parameters. Numbers and arrows correspond to descriptions in the text. Pulses are marked with red and purges are marked with blue. (For interpretation of the references to colour in this figure legend, the reader is referred to the web version of this article.)

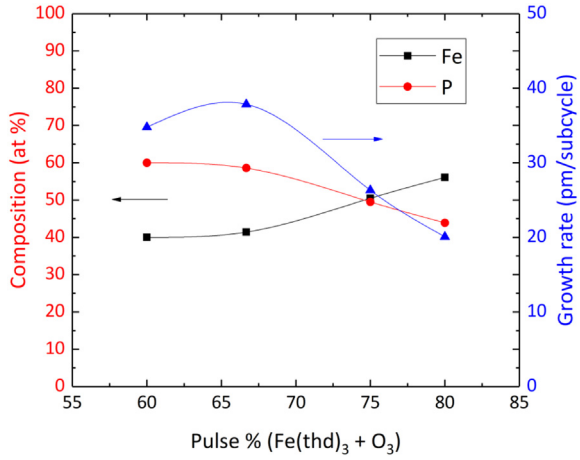

Fig. 3. Composition of iron (black) and phosphorus (red) in the deposited thin films and growth rate (blue) vs pulsing percentage of $Fe(thd)_3 + O_3$, obtained from XRF measurements and spectroscopic ellipsometry. (For interpretation of the references to colour in this figure legend, the reader is referred to the web version of this article.)

the thin films alone, with minimal contributions from redox reactions and mostly non-Faradic contribution. There are no clearly visible redox peaks in the voltammogram of the 1 nm film, confirming a non-Faradic behavior. Its response fits well into the 30 nm curve, and we can assume that the 1 nm film approximately corresponds to the non-Faradic contribution of the system, more on this later.

To observe how the capacity of the materials varied with different applied currents we performed galvanostatic cycling. When studying $Fe_4(P_2O_7)_3$, we discovered that the 10 nm film had significantly higher area capacity than the 150 nm film, Fig. 8(a), despite the difference in mass. The 10 nm film reached an area capacity of approximately 0.5 μAh/cm^2 while the 150 nm film never exceeded 0.2 μAh/cm^2. The specific capacity the 10 nm film was slightly higher than 100 mAh/g, which is approaching the theoretical capacity of 144 mAh/g. The 10 nm film shows good cycling stability and can handle currents up to 2560 μA while still showing electrochemical capacity. The capacity of the 150 nm is more sensitive towards higher currents. During the measurements in Fig. 8, the 10 nm film shows a small increase in capacity, indicating a self-enhancing mechanism. This could mean that the material creates new and better pathways for lithium intercalation, as indicated in previous studies [6,14,15].

The corresponding experiments for $FePO_4$, Fig. 9, show similar trends as for $Fe_4(P_2O_7)_3$. The thinner films exhibit higher capacity and better stability at higher currents compared to the thicker films. Poor

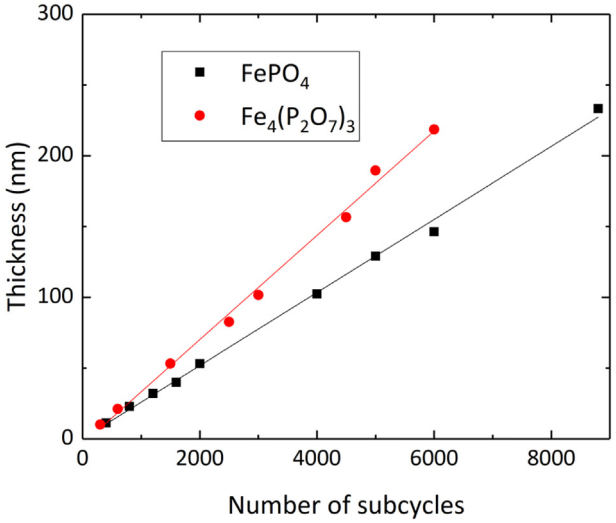

Fig. 4. Thickness of deposited thin films of $Fe_4(P_2O_7)_3$ (red) and $FePO_4$ (black) as a function of number of subcycles. (For interpretation of the references to colour in this figure legend, the reader is referred to the web version of this article.)

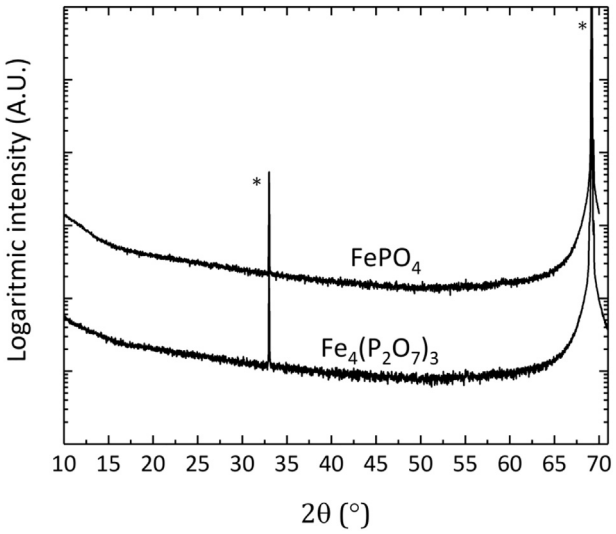

Fig. 5. Results from XRD measurements of a 180 nm thin film of $Fe_4(P_2O_7)_3$ and a 135 nm $FePO_4$ thin film. * marks the peaks obtained from the silicon substrate. The y-axis is given in a logarithmic scale to enhance small features.

conductivity of the iron phosphates is probably the reason why the thicker films perform worse than the thinner [16]. The difference between the two materials is that $FePO_4$ has a significantly higher capacity than $Fe_4(P_2O_7)_3$. A 10 nm $FePO_4$ reaches an area capacity of 1.0 μAh/cm^2, which is approximately twice that of $Fe_4(P_2O_7)_3$. When comparing the area capacity of the 20 and 10 nm $FePO_4$, we observe that the 20 nm film has a higher capacity at lower currents, while 10 nm shows the highest capacity at higher currents. The 10 nm film is the only film that has significant capacity at 5120 μA, where it exhibits a specific capacity of 30 mAh/g. These results are in line with those previously obtained by Gandrud et al. [6,7], however, while we have currently corrected for surface roughness of the substrates, this is not mentioned in the prior work.

At 20 and 2 μA, the 10 nm $FePO_4$ film showed a maximum in capacity of 184 and 235 mAh/g, respectively. These values are significantly higher than the theoretical capacity of 178 mAh/g and cannot stem from inaccuracies in calculation of the cathode mass alone. Since the films are very thin, reactions on the surface of the cathode can become a significant part of the contribution to the total capacity. In an attempt to measure this non-Faradaic capacity, we performed GC measurements on a 1 nm thin film, which corresponds (more or less) to an $FePO_4$ surface alone. As we can see from Fig. 10, the 1 nm film shows a significant capacity (0.4 μAh/cm^2 at 20 μA) compared to the reference battery with an uncoated steel spacer as cathode, showing the importance of the non-Faradaic capacity. The 1 nm film does not show a similar self-enhancing mechanism as for the 10 nm film throughout its campaign.

We performed cycle life measurements at 80 μA for the $FePO_4$ films to obtain a better understanding on how the capacity changed over time. From Fig. 11, we can see that all thicknesses, except for 1 nm, experience an increase in capacity during early cycling stages, due to the self-enhancing mechanism. However, the increase is dependent on the film thickness, where the 40, 20 and 10 nm films experience an increase of 240, 150 and 90%, respectively. In addition, the thicker films need more time to reach peak capacity, where the 150 nm film still has not reached a clear peak even after 8000 cycles. The 1 nm film, representing the non-Faradaic capacity, is very stable at around 0.3 μAh/cm^2 throughout the campaign.

Because the capacity varies differently over time for different thicknesses, it is difficult to derive a fixed correlation between the capacity and the thickness. In Fig. 12, we have plotted data points for all the thicknesses from the 80 μA cycle life measurements, at three different cycle numbers. The dependency is very sensitive to which points we choose, enabling that the 150 nm film goes from having the lowest capacity to the highest capacity by choice of data points. The peak capacity for the 150 nm is taken from cycle number 20000, which is not included in Fig. 11. Even after that many cycles the capacity of the 150 nm film still continues to increase. We do speculate that if it had reached its true peak capacity we may have obtained a linear dependency between the peak capacity and the thickness. However, within a reasonable time scale we can conclude that the area capacity, at moderate currents, increases with thickness up to approximately

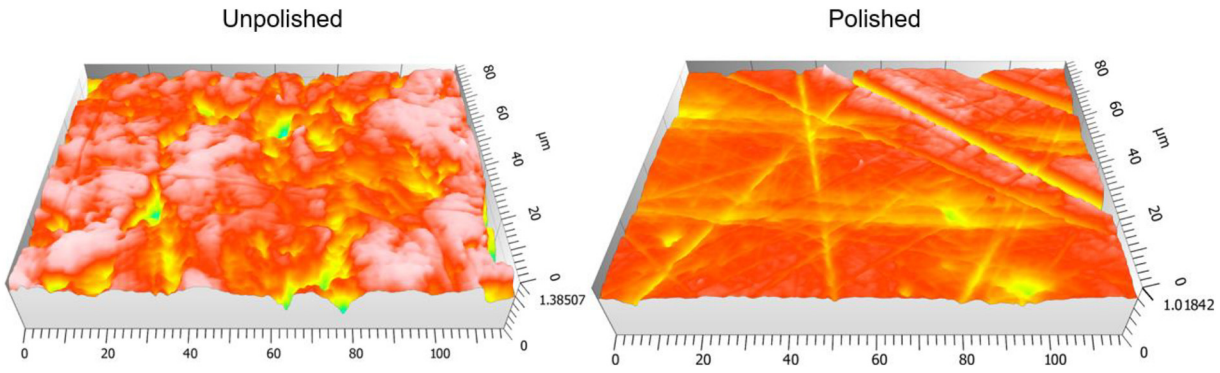

Fig. 6. Topography of unpolished (left) and polished (right) steel spacers, used as substrates for electrochemical characterization of iron phosphate thin films.

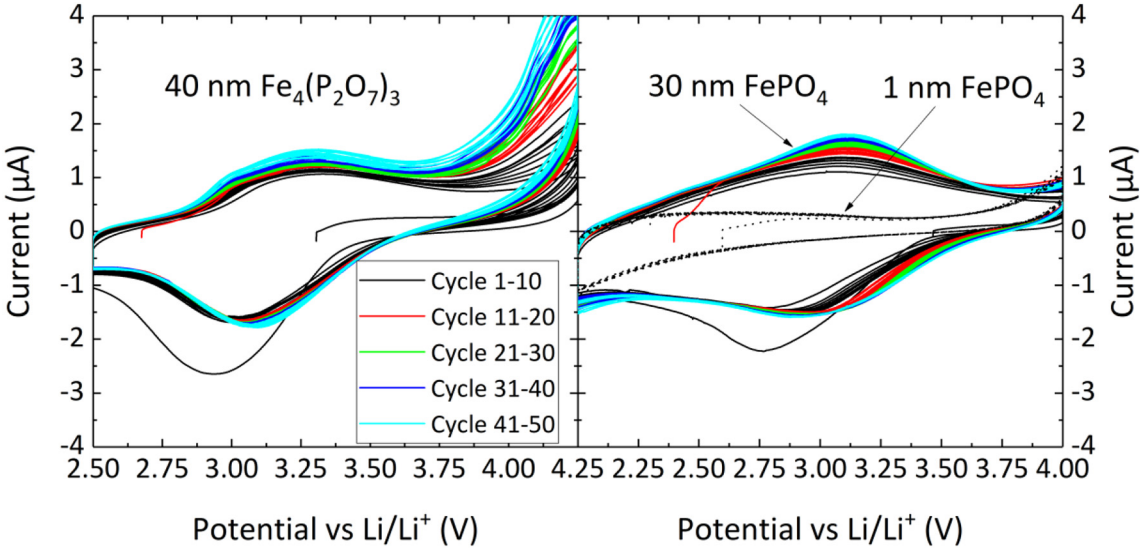

Fig. 7. Cyclic voltammograms of 40 nm $Fe_4(P_2O_7)_3$ and 30 nm $FePO_4$ compared to 1 nm $FePO_4$ corresponding to the non-Faradic contribution, measured with a sweep rate of 0.1 mV/s.

40 nm before it stabilizes or decreases. With regards to specific capacity, the thinnest films have the highest value.

One might be tempted to subtract the non-Faradaic capacity from the total capacity to determine the contribution from the redox reactions alone (Faradaic capacity), but this will not necessarily be correct. As we can see from Fig. 11(a) the non-Faradaic capacity is larger than the total capacity of the 150 nm film in the beginning. This is a clear sign that the non-Faradaic capacity acts differently for different film thicknesses and might also change during cycling. The non-Faradaic capacity is probably larger for thinner films than for thicker films considering the limited electronic conductivity of the deposited material. The non-Faradaic capacity of 0.3 μAh/cm^2 for the 1 nm film might be exaggerated because of potential redox reactions in the 1 nm film as well. However, this Faradaic capacity should at maximum correspond to 0.1 μAh/cm^2 (1/10 of the 10 nm peak capacity). On the basis of measurements at 2 μA of 10 and 1 nm film, we obtained a peak capacity of 235 mAh/g for the 10 nm film. When we subtracted the capacity from the 1 nm film (non-Faradaic capacity) we calculated the Faradaic capacity to be as low as 109 mAh/g. There are uncertainties related to these calculations, but it shows that the non-Faradaic capacity is significant for thin films and that one should be careful when comparing the obtained capacities with the theoretical capacity.

4. Conclusions

In this work, we have confirmed the good electrochemical properties of amorphous $FePO_4$ thin films as cathode material with very good power capabilities and good cycle life. We have proved that the electrochemical properties of amorphous $Fe_4(P_2O_7)_3$ behave similar to $FePO_4$, although with less capacity. Through characterizations of a 1 nm thick $FePO_4$ film, we have identified the non-Faradaic capacity of the thin films and proven its significance when determining the overall capacity of a thin film cathode material.

Abbreviations

ALD	atomic layer deposition
CV	cyclic voltammetry
DMC	dimethyl carbonate
EC	ethylene carbonate

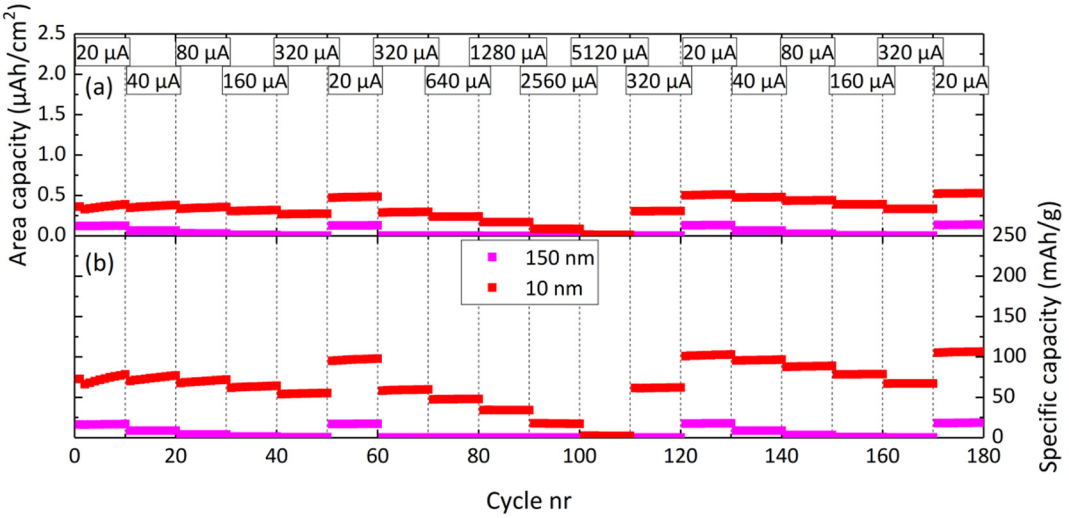

Fig. 8. (a) Area capacity and (b) specific capacity obtained from GC measurements of thin film $Fe_4(P_2O_7)_3$ with a voltage range of 2.50–4.25 V and currents ranging from 20 to 5120 μA.

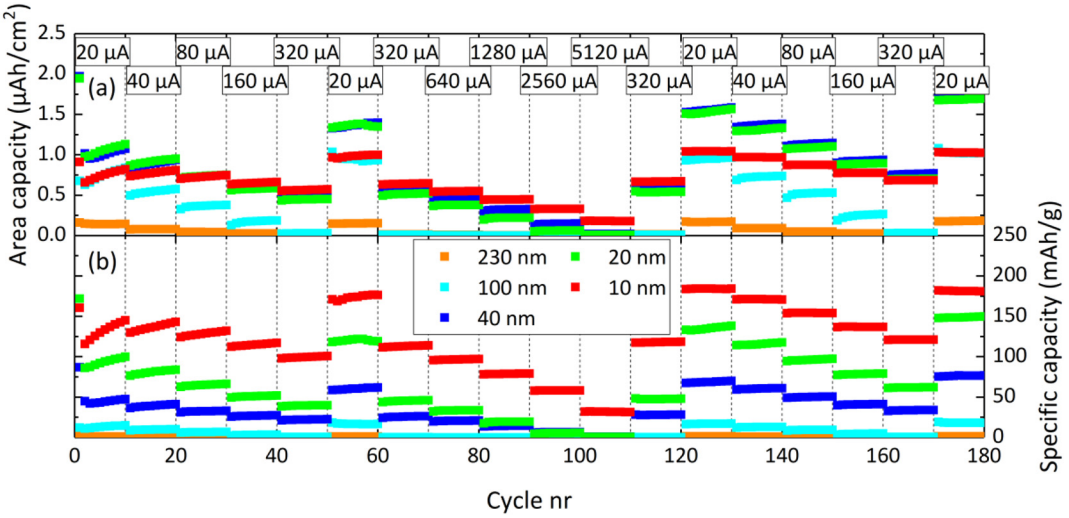

Fig. 9. (a) Area capacity and (b) specific capacity obtained from GC measurements of thin film $FePO_4$ with a voltage range of 2.0–4.0 V and currents ranging from 20 to 5120 µA.

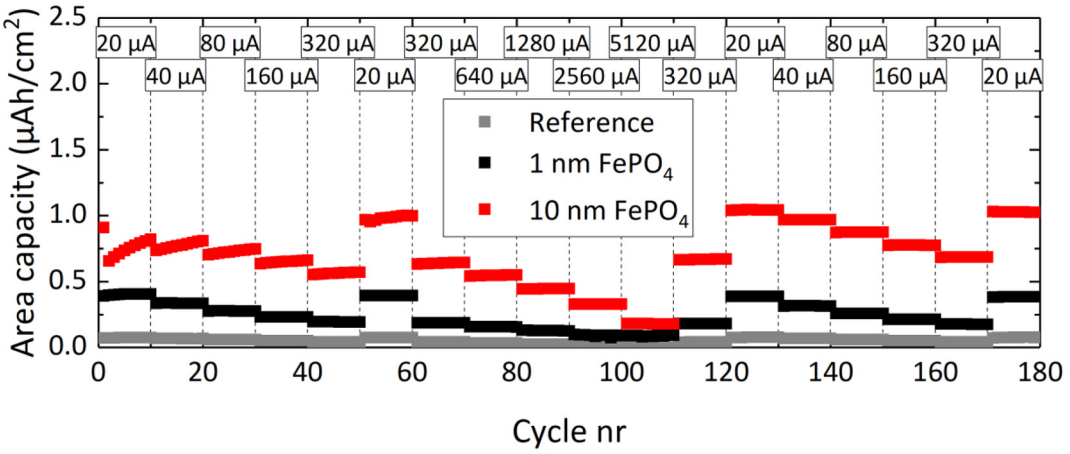

Fig. 10. Area capacity vs cycle number of reference battery (gray), average of four measurements of 1 nm $FePO_4$ (black) representing the non-Faradaic capacity and 10 nm $FePO_4$ (red). (For interpretation of the references to colour in this figure legend, the reader is referred to the web version of this article.)

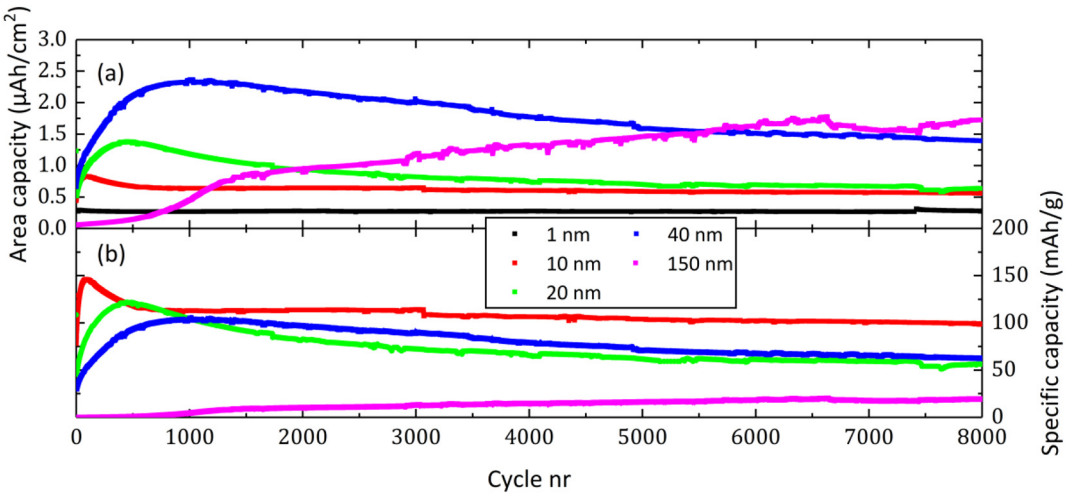

Fig. 11. (a) Area capacity and (b) specific capacity obtained from GC cycle life measurements of different thicknesses of $FePO_4$ thin films. Measurements are performed at 80 µA with a voltage range of 2.0–4.0 V.

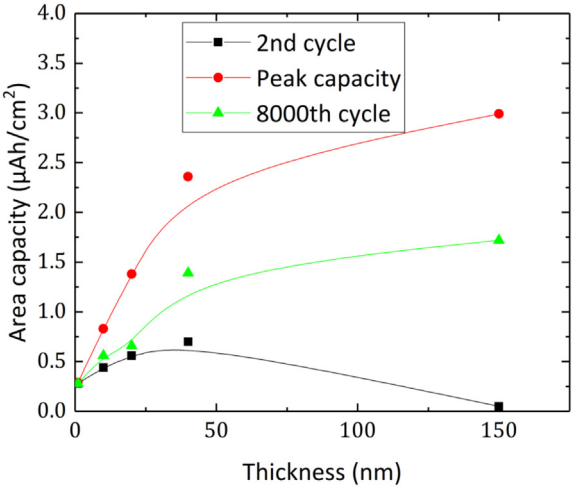

Fig. 12. Area capacity vs thickness obtained from 2nd cycle, peak capacity and 8000th cycle from the 80 μA cycle life measurements. The peak capacity for the 150 nm film is taken from cycle number 20000, which is not included in Fig. 11.

GC	galvanostatic cycling
XRD	X-ray diffraction
XRF	X-ray fluorescence
LFP	$LiFePO_4$
QCM	quartz crystal microbalance

Author contributions

The manuscript was written through contributions of all authors. All authors have given approval to the final version of the manuscript.

Funding sources

This work was supported by the Research Council of Norway through project number 262387 Solid state electrolytes for all-solid thin film Li-ion batteries.

CRediT authorship contribution statement

Anders Brennhagen: Methodology, Formal analysis, Investigation, Writing - original draft, Visualization.**Kristian B. Kvamme:**Methodology, Validation, Writing - review & editing, Supervision.**Katja S.S. Sverdlilje:**Methodology, Software, Validation, Writing - review & editing, Supervision.**Ola Nilsen:**Conceptualization, Software, Resources, Writing - review & editing, Supervision, Project administration, Funding acquisition.

Declaration of competing interest

The authors declare that they have no known competing financial interests or personal relationships that could have appeared to influence the work reported in this paper.

Acknowledgment

We are grateful for Senior Engineer Alejandro Barrantes Bautista's help with topography measurements on the optical profiler at the Department of Odontology. We would also like to thank Knut Bjarne Gandrud for helpful discussions.

References

[1] L.-X. Yuan, Z.-H. Wang, W.-X. Zhang, X.-L. Hu, J.-T. Chen, Y.-H. Huang, J.B. Goodenough, Development and challenges of $LiFePO_4$ cathode material for lithium-ion batteries, Energy Environ. Sci. 4 (2011) 269–284.
[2] Y. Lu, Q. Zhang, J. Chen, Recent progress on lithium-ion batteries with high electrochemical performance, Sci. China Chem. 62 (2019) 533–548.
[3] A. Eftekhari, $LiFePO_4$/C nanocomposites for lithium-ion batteries, J. Power Sources 343 (2017) 395–411.
[4] D. Choi, P.N. Kumta, Surfactant based sol–gel approach to nanostructured LiFePO4 for high rate Li-ion batteries, J. Power Sources 163 (2007) 1064–1069.
[5] P.P. Prosini, M. Carewska, S. Scaccia, P. Wisniewski, M. Pasquali, Long-term cyclability of nanostructured $LiFePO_4$, Electrochim. Acta 48 (2003) 4205–4211.
[6] K.B. Gandrud, O. Nilsen, H. Fjellvåg, Ultra-high power capabilities in amorphous $FePO_4$ thin films, J. Power Sources 306 (2016) 454–458.
[7] K.B. Gandrud, A. Pettersen, O. Nilsen, H. Fjellvåg, High-performing iron phosphate for enhanced lithium ion solid state batteries as grown by atomic layer deposition, J. Mater. Chem. A 1 (2013) 9054–9059.
[8] L. Zhang, M.E. Schlesinger, R.K. Brow, Phase Equilibria in the Fe_2O_3–P_2O_5 system, J. Am. Ceram. Soc. 94 (2011) 1605–1610.
[9] Y.-S. Hong, Y.J. Park, K.S. Ryu, S.H. Chang, Crystalline Fe_3PO_7 as an electrode material for lithium secondary batteries, Solid State Ionics 156 (2003) 27–33.
[10] R. Baies, V. Pralong, V. Caignaert, B. Raveau, Soft chemistry synthesis, structure and electrochemical characterization of iron phosphates $Fe(H_2PO_4)_3$ and $Fe(PO_3)_3$, Mater. Res. Bull. 41 (2006) 1170–1177.
[11] M.D. Bhatt, J.Y. Lee, High capacity conversion anodes in Li-ion batteries: a review, Int. J. Hydrog. Energy 44 (2019) 10852–10905.
[12] S.-i. Nishimura, M. Nakamura, R. Natsui, A. Yamada, New lithium iron pyrophosphate as 3.5 V class cathode material for lithium ion battery, J. Am. Chem. Soc. 132 (2010) 13596–13597.
[13] M. Diskus, O. Nilsen, H. Fjellvåg, Growth of thin films of molybdenum oxide by atomic layer deposition, J. Mater. Chem. 21 (2011) 705–710.
[14] C.-L. Li, B. Zhang, Z.-W. Fu, Physical and electrochemical characterization of thin films of iron phosphate and nitrided iron phosphate for all-solid-state batteries, J. Electrochem. Soc. 153 (2006) E160–E165.
[15] H. Kim, S.-W. Kim, J. Hong, H.-D. Lim, H.S. Kim, J.-K. Yoo, K. Kang, Graphene-based hybrid electrode material for high-power lithium-ion batteries, J. Electrochem. Soc. 158 (2011) A930–A935.
[16] T.K. Pietrzak, L. Wewior, J.E. Garbarcyk, M. Wasiucionek, I. Gorzkowska, J.L. Nowinski, S. Gierlotka, Electrical properties and thermal stability of FePO4 glasses and nanomaterials, Solid State Ionics 188 (2011) 99–103.